Mineralogical Magazine (2024), **88**, 473–481
doi:10.1180/mgm.2024.29

CAMBRIDGE UNIVERSITY PRESS

Article

Atomic-scale deformation mechanisms at high-pressure in inderborite, $CaMg[B_3O_3(OH)_5]_2(H_2O)_4{\cdot}2H_2O$

Davide Comboni[1], Tommaso Battiston[1], Paolo Lotti[1], Michael Hanfland[2] and G. Diego Gatta[1]

[1]Dipartimento di Scienze della Terra, Università degli Studi di Milano, Via Botticelli 23, 20133 Milano, Italy; and [2]ESRF – European Synchrotron Radiation Facility, 71 Avenue des Martyrs, CS 40220, 38043 Grenoble Cedex 9, France

Abstract

The high-pressure behaviour of inderborite [ideally $CaMg[B_3O_3(OH)_5]_2(H_2O)_4{\cdot}2H_2O$, space group $C2/c$ with $a \approx 12.14$, $b \approx 7.43$, $c \approx 19.23$ Å and $\beta \approx 90.3°$ at room conditions] has been studied by two *in situ* single-crystal synchrotron X-ray diffraction experiments up to ~10 GPa, using He as pressure-transmitting fluid. Between 8.11(5) and 8.80(5) GPa, inderborite undergoes a first-order phase transition to its high-pressure polymorph, inderborite-II (with $a \approx 11.37$, $b \approx 6.96$, $c \approx 17.67$ Å, $\beta \approx 96.8°$ and $\Delta V \approx 7.0\%$, space group unknown). The isothermal bulk modulus ($K_{V0} = \beta^{-1}_{P0,T0}$, where $\beta_{P0,T0}$ is the volume compressibility coefficient) of inderborite was found to be $K_{V0} = 41(1)$ GPa. The destructive nature of the phase transition prevented any structure resolution of inderborite-II or even the continuation of the experiments at pressures higher than 10.10(5) GPa. In the pressure range 0–8.11(5) GPa, the compressional anisotropy of inderborite, indicated by the ratio between the principal components of the Eulerian finite unit-strain ellipsoid, is $\varepsilon_1:\varepsilon_2:\varepsilon_3 = 1.4:1.05:1$. The deformation mechanisms at the atomic scale in inderborite are here described. Our findings support the hypothesis of a quasi-linear correlation between the total H_2O content and *P*-stability range in hydrated borates, as the pressure at which inderborite undergoes the phase transition falls in line with most of the hydrate borates studied at high-pressure so far.

Keywords: inderborite; high-pressure; single crystal X-ray diffraction; elastic compressibility; phase transition

(Received 21 February 2024; accepted 9 April 2024; Accepted Manuscript published online: 22 May 2024)

Introduction

Boron is a strategic element used in a variety of products, including ant poisons, detergents (for bleaching), borosilicate glasses (such as Pyrex®), and ceramics (Abe, 1952; Woods, 1994; Klotz and Moss, 1996; Yu *et al.*, 2018; Chen *et al.*, 2020; U.S.G.S, 2022). The strategic importance of boron, and the moderate supply risk due to its uneven distribution, has been recognised by the European Union, which has classified borates as critical raw material since 2014 (European Commission, 2014). Economically viable boron mineral deposits are distributed irregularly worldwide and are mostly represented by five main hydrated borate minerals: ulexite, colemanite, borax, tincalconite and kernite (Kistler and Helvacı, 1994; Helvaci and Alonso, 2000; Zheng *et al.*, 2005; García-Veigas and Helvacı, 2013). Other borate minerals, such as inderborite, meyerhofferite, inyoite and tertschite, are often found in smaller weight fractions alongside these main minerals. Due to their low production cost, hydrated borates are believed to be good candidates as aggregates in neutron shielding concretes (Okuno, 2005; Okuno *et al.*, 2009; Glinicki *et al.*, 2018), because of the ^{10}B isotope (which accounts for ~20% of natural boron) high cross-section for thermal neutrons (~3840 barns) (Carter *et al.*, 1953; Palmer and Swihart, 1996), leading to the reaction:

$$^{10}B + n \rightarrow \alpha + ^{7}Li + \gamma.$$

Inderborite, ideally $CaMg[B_3O_3(OH)_5]_2(H_2O)_4{\cdot}2H_2O$, space group $C2/c$ with $a \approx 12.14$, $b \approx 7.43$, $c \approx 19.23$ Å and $\beta \approx 90.3°$, was originally discovered at the Inder Lake borate deposit, western Kazakhstan, and later also at the Eskişehir district, Turkey (Kurkutova *et al.*, 1965; Palmer and Helvaci, 1997). The lower occurrence of inderborite, with respect to other most common borates, is attributed to its extremely narrow stability field in the $CaO–MgO–B_2O_3–H_2O$ system, as demonstrated by Birsoy and Özbaş (2012). However, minor fractions of inderborite are commonly found associated with colemanite and ulexite in valuable ore deposits of hydrate borates (*e.g.* Kirka and Sarikaya deposits) (Palmer and Helvaci, 1997; Helvacı and Palmer, 2017). For example, inderborite has been found in the ore debris near the Kuşkaya gallery of the Turkish Borax Mining Company, in the Sarikaya borate deposits, alongside other borate minerals such as colemanite, borax, ulexite, kurnakovite and inderite (Baysal, 1973).

Kurkutova *et al.* (1965) were the first to determine the crystal structure of inderborite (Fig. 1), although the complex hydrogen bond network was only described later by Burns and Hawthorne (1994). In a recent paper, based on a multi-methodological approach, the crystal chemistry (with a focus on

Corresponding author: Davide Comboni; Email: davide.comboni@unimi.it
Associate Editor: Sergey V Krivovichev
Cite this article: Comboni D., Battiston T., Lotti P., Hanfland M. and Gatta G.D. (2024) Atomic-scale deformation mechanisms at high-pressure in inderborite, $CaMg[B_3O_3(OH)_5]_2(H_2O)_4{\cdot}2H_2O$. *Mineralogical Magazine* **88**, 473–481. https://doi.org/10.1180/mgm.2024.29

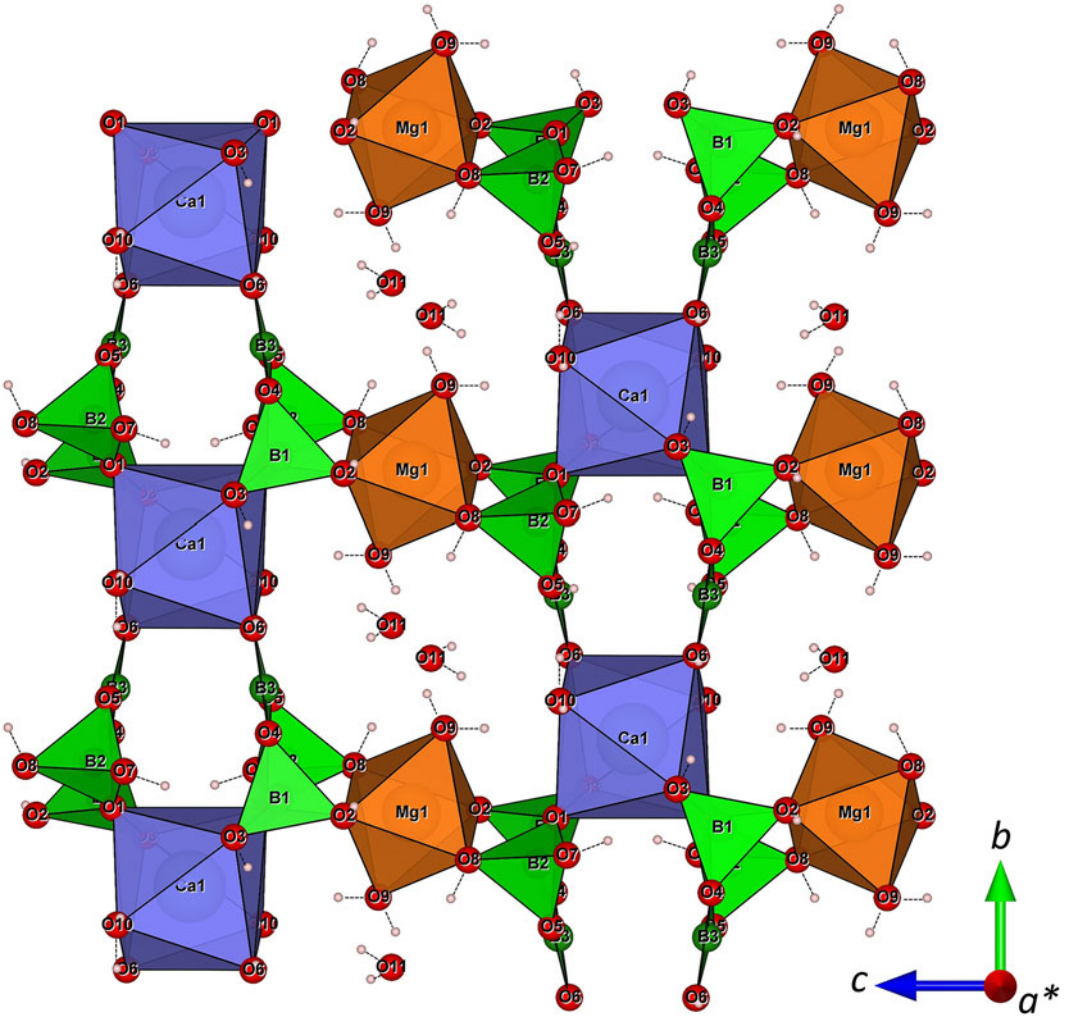

Figure 1. Inderborite structure, based on the model proposed by Gatta *et al.* (2023), viewed perpendicular to the (100) plane. Ca-polyhedrons in indigo, Mg-polyhedrons in orange, boron polyhedrons in green, hydrogen in small pale pink spheres. Drawn using *VESTA* software (Momma and Izumi, 2008),

the B isotopic composition) and structure of inderborite (based on a single-crystal neutron diffraction experiment) were re-investigated by Gatta *et al.* (2023). They confirmed that the chemical composition of the inderborite from Inder, Kazakhstan is virtually identical to the ideal one. The fundamental building block (FBB) of inderborite is a $[B_3O_3(OH)_5]^{2-}$ ring, consisting of 2 $B\varphi_4$ tetrahedrons and one planar trigonal $B\varphi_3$ unit (φ represents an O^{2-} anion, an OH^- hydroxyl group or a H_2O molecule). The same <Δ2□> unit (Δ stands for a $B\varphi_3$ unit, and □ for a $B\varphi_4$ tetrahedron), in which all oxygen atoms that are not shared between two boron atoms are protonated (Burns and Hawthorne, 1994), occurs also in kurnakovite, meyerhofferite, inyoite, inderite and solongoite, whereas in hydroboracite and colemanite it is polymerised into chains (Hawthorne, 2012). In the crystal structure of inderborite, the $[B_3O_3(OH)_5]^{2-}$ rings are interconnected with the Ca-polyhedra and Mg-octahedra through the O1, O2, O3, O6 and O8 oxygen hinges. This results in the formation of continuous heteropolyhedral sheets parallel to (100) (Fig. 1), connected through a complex hydrogen bonding network involving O7 and O4 as *acceptors*, respectively from the O3 and O6 hydroxyl groups and from the O10 H_2O molecule. A crucial role in providing stability to the crystal structure is attributed to the interstitial ('zeolitic') H_2O molecule O11, which occupies a key position between the sheets (Fig. 1). O11 is connected, via hydrogen bonding, to O8 and O9: the former is an oxygen hinge that connects the Mg-octahedron with the B2-tetrahedron, whereas the latter is a H_2O molecule belonging only to the Mg-octahedron. This further connects the crystal structure along the [010] crystallographic direction. O9 is also a *donor* to O10, the only H_2O molecule of the complex Ca polyhedrons, providing the only weak connection between Ca- and Mg-polyhedrons.

At the present time, inderborite remains an extremely poorly studied mineral. The only available Raman spectrum to date can be found on the https://rruff.info/ website, and some important thermodynamic parameters (such as the thermal expansion coefficient and elastic compressibility) are still missing. As pointed out by Gatta *et al.* (2023), given the importance of the hydrogen bonding network in inderborite, a compressional, thermal, or chemical perturbation of the H-bonding scheme could easily lead to a phase transition. On this basis, in this study we aim to: (1) assess the stability range of inderborite with respect to pressure, including for potential industrial utilisation of this borate; and (2) describe the structural evolution of

https://doi.org/10.1180/mgm.2024.29 Published online by Cambridge University Press

inderborite, at the atomic scale, with increasing pressure. While inderborite is not likely to be used as primary component in radiation shielding concretes, its association with major hydrated borates (*e.g.* colemanite and borax) makes it imperative to investigate its stability under non-ambient conditions. Furthermore, its stability at high-pressure allows (3) comparisons to be drawn with other hydrated borate structures studied and to strengthen the hypothesis of a correlation between the total H_2O content and the stability range of hydrated borates under pressure.

Experimental procedures

The sample of inderborite used in this study comes from the type locality (Inder Deposit, Kazakhstan), and was provided by the late Dr. Renato Pagano. Crystals from the same sample were recently used for the experiments reported by Gatta *et al.* (2023). Inderborite is a light (1.92 g/cm^3) and soft (3.5 on the Mohs scale) mineral with a prismatic habit. Two single crystals, each measuring ~20×15×10 μm, were selected for high-pressure experiments at the ID15b beamline, ESRF, Grenoble, France. The diffraction experiment employed a convergent monochromatic beam ($E \approx 30$ keV, $\lambda \approx 0.41$ Å and ~200 mA). Helium was used as the pressure-transmitting fluid (Klotz *et al.*, 2009), and two ruby micro-spheres were added as pressure calibrants (pressure uncertainty ± 0.05 GPa; Mao *et al.*, 1986). The crystals were loaded in two different membrane-driven DACs (diamond anvil cells), with 600 μm culet Boehler-Almax design anvils. For each DAC, a stainless-steel foil (with thickness of ~250 μm) was pre-indented to ~80 μm and then drilled by spark-erosion, leading to a *P*-chamber of ~300 μm in diameter. The diffraction patterns were collected by an Eiger2X 9M detector, positioned ~180 mm from the sample. The sample-to-detector distance was calibrated using a Si standard and a vanadinite ($Pb_5(VO_4)_3Cl$) single crystal. A pure ω-scan ($-32° \leq \omega \leq +32°$) was used to collect the diffraction patterns, with a 0.5° step width and a 0.5 s exposure time per step. Further details on the beamline setup can be found in Hanfland (2016) and Poreba *et al.* (2022).

Data analysis

The *CrysAlisPro* package (Rigaku Oxford Diffraction, 2019) was used to index the diffraction peaks and integrate their intensities; corrections for Lorentz-polarisation effects were also applied. The semi-empirical *ABSPACK* routine, implemented in *CrysAlisPro*, was used to account for X-ray absorption effects caused by the DAC components. Table 1 lists the unit-cell parameters at high pressure, and their evolution with *P* is shown in Fig. 2. Selected diffraction patterns are also presented in Fig. 3. The *JANA2006* package (Petrícek *et al.*, 2014) was used for all structure refinements, with the initial fractional coordinates taken from Burns and Hawthorne (1994) and Gatta *et al.* (2023). The CIFs (crystallographic information files) are deposited as supplementary materials (see below).

High-pressure data were collected up to 9.84(5) GPa, as the number and intensity of the observed reflections [*i.e.* with $F_o^2 > 3\sigma(F_o^2)$] decreased significantly after the phase transition at 8.80(5) GPa (as Fig. 3 shows), effectively ending the experiment. In both the experiments, crystals did not recover after the phase transition. This was the most destructive phase transition observed in hydrated borates to date (compare Comboni *et al.*, 2020b, 2022a), as the number of observed reflections was barely enough to properly index the diffraction pattern of the high-pressure polymorph, inderborite-II, which was found to be metrically monoclinic. The space group has not been unambiguously determined.

Table 1. Evolution of the unit-cell parameters of inderborite with pressure obtained from the two independent experiments (*high-pressure polymorph).

P (GPa)	*a* (Å)	*b* (Å)	*c* (Å)	β (°)	*V* (Å^3)
First dataset					
0.0001	12.1300(5)	7.4253(2)	19.1940(4)	90.324(6)	1728.80(7)
0.43(5)	12.0977(4)	7.4114(6)	19.1495(3)	90.332(3)	1716.9(2)
0.61(5)	12.0820(4)	7.4028(6)	19.1256(3)	90.351(3)	1710.6(2)
1.19(5)	12.0212(4)	7.3744(6)	19.0295(3)	90.382(3)	1686.9(4)
1.80(5)	11.9696(5)	7.3425(7)	18.9417(4)	90.418(4)	1664.7(2)
2.35(5)	11.9198(4)	7.3170(6)	18.8554(3)	90.444(3)	1644.5(4)
2.82(5)	11.8804(4)	7.2925(6)	18.7842(3)	90.457(3)	1627.4(4)
3.33(5)	11.8361(4)	7.2664(6)	18.6986(3)	90.483(3)	1608.1(4)
3.84(5)	11.8093(4)	7.2487(6)	18.6366(4)	90.534(3)	1595.3(2)
4.54(5)	11.7653(4)	7.2194(7)	18.5425(4)	90.566(3)	1574.9(2)
6.23(5)	11.6781(5)	7.1664(7)	18.3259(4)	90.629(4)	1533.6(2)
7.08(5)	11.6443(5)	7.1444(7)	18.2319(4)	90.638(3)	1516.7(2)
7.80(5)	11.6192(5)	7.1256(8)	18.1556(4)	90.629(3)	1503.1(2)
8.11(5)	11.5986(5)	7.1162(8)	18.1089(4)	90.623(3)	1494.6(2)
8.80(5)*	11.37(1)	6.964(5)	17.672(12)	96.8(2)	1390(6)
10.10(5)*	11.49(1)	6.99(2)	17.33(4)	95.7(2)	1385(6)
Second dataset					
0.0001	12.139(6)	7.4286(3)	19.1975(5)	90.352(6)	1731.2(8)
0.35(5)	12.110(5)	7.4128(2)	19.1484(5)	90.371(6)	1718.9(8)
0.86(5)	12.065(6)	7.3902(2)	19.0812(5)	90.402(6)	1701.3(8)
1.56(5)	12.008(5)	7.3589(2)	18.9832(5)	90.402(7)	1677.4(8)
2.32(5)	11.931(7)	7.3231(3)	18.8708(6)	90.425(8)	1648.7(10)
3.05(5)	11.875(6)	7.2868(3)	18.7546(6)	90.515(7)	1622.8(8)
3.81(5)	11.830(6)	7.2477(3)	18.6346(5)	90.516(7)	1597.7(8)
4.67(5)	11.802(6)	7.2110(3)	18.5194(6)	90.592(7)	1575.9(8)
5.30(5)	11.764(7)	7.1928(3)	18.4533(7)	90.636(9)	1561.4(9)
6.20(5)	11.719(6)	7.1655(3)	18.3571(6)	90.555(8)	1541.4(8)
6.90(5)	11.674(7)	7.1460(3)	18.2757(7)	90.603(9)	1524.5(10)
7.45(5)	11.654(7)	7.1305(3)	18.2115(6)	90.638(9)	1513.3(9)
8.96(5)*	11.435(2)	6.932(8)	17.453(12)	96.05(8)	1375(2)

Relevant interatomic distances, average bond lengths, angles, polyhedral volumes, distortion index [defined as $D = \frac{1}{n}\sum_{i=1}^{n}\frac{|l_i - l_{av}|}{l_{av}}$, where l_i is the distance from the central atom to the i^{th} coordinating atom, and $l_{av}$is the average bond length; Baur, 1974], quadratic elongation [defined as $\langle\lambda\rangle = \frac{1}{n}\sum_{i=1}^{n}\left(\frac{l_i}{l_0}\right)^2$, where l_0 is the center-to-vertex distance of a regular polyhedron of the same volume and l_i is the actual centre-to-vertex length; Robinson *et al.*, 1971] and bond angle variance [defined as $\sigma^2 = \frac{1}{m-1}\sum_{i=1}^{m}(\phi_i - \phi_0)^2$ where *m* is the number of faces in the polyhedron×3/2, *i.e.* number of bond angles, ϕ_i is the i^{th} bond angle, and ϕ_0 is the ideal bond angle for a regular polyhedron *e.g.* 90° for an octahedron; Robinson *et al.*, 1971] have been calculated using the tools implemented in the *VESTA* software (Momma and Izumi, 2008), and are listed in Supplementary Table S1. Relevant interatomic angles and distances are reported in Table 2.

To describe the isothermal behaviour of inderborite, a second-order Birch–Murnaghan Equation of State (BM–EoS) was fitted to the *P*–*V* data (Birch, 1947). This EoS allows refinement of the bulk modulus [K_{V0} or $K_{P0,T0}$, defined as $-V_0(\partial P/\partial V)_{T0} = \beta^{-1}{}_{P0,T0}$, where $\beta_{P0,T0}$ is the volume compressibility coefficient at room conditions] and its *P*-derivatives [$K' = \partial K_{P0,T0}/\partial P$

https://doi.org/10.1180/mgm.2024.29 Published online by Cambridge University Press

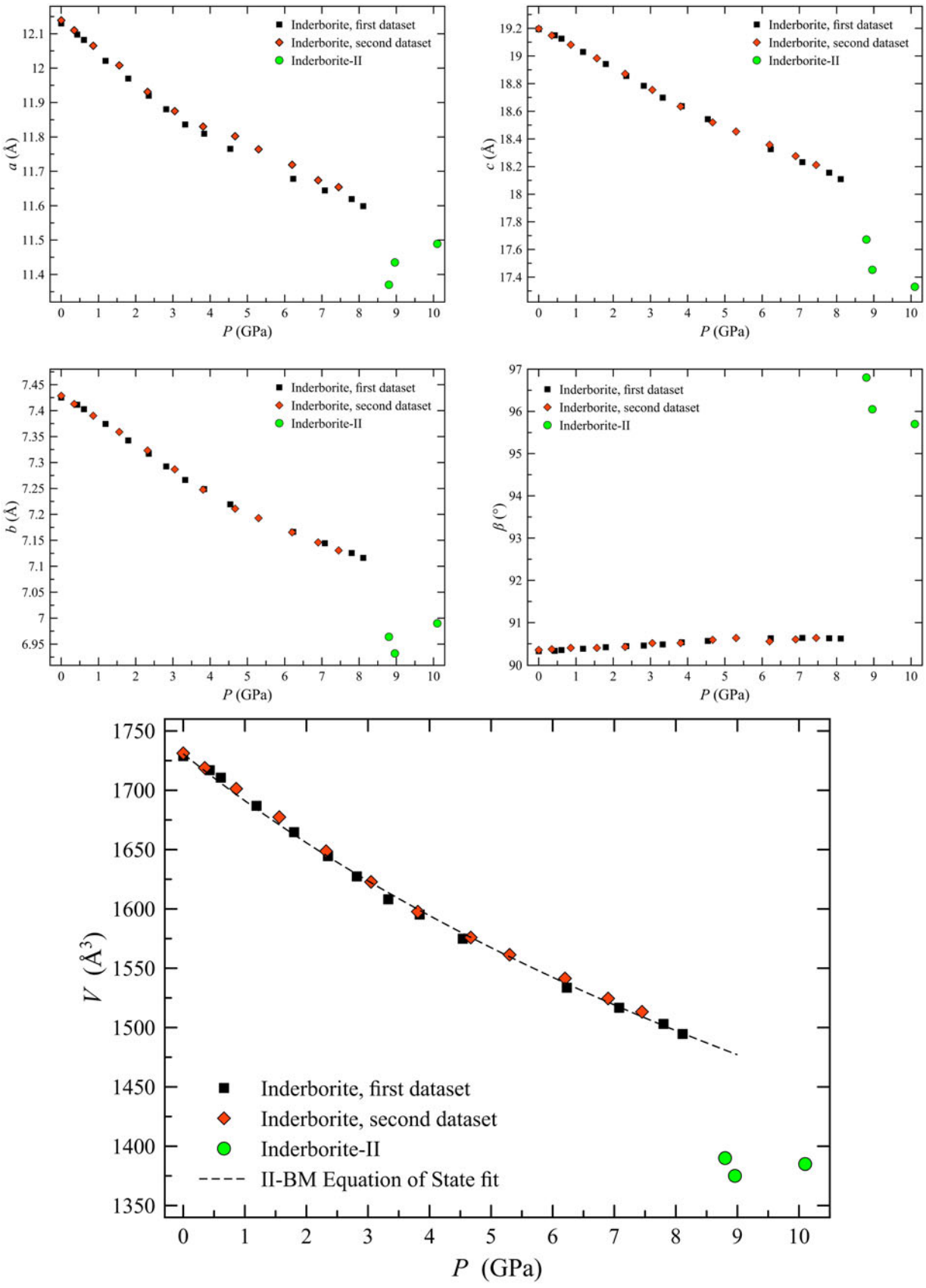

Figure 2. Evolution with pressure of the unit-cell parameters of inderborite: first dataset in black squares, second dataset in red diamonds, inderborite-II in green circles. Estimated standard deviations are smaller than symbols.

https://doi.org/10.1180/mgm.2024.29 Published online by Cambridge University Press

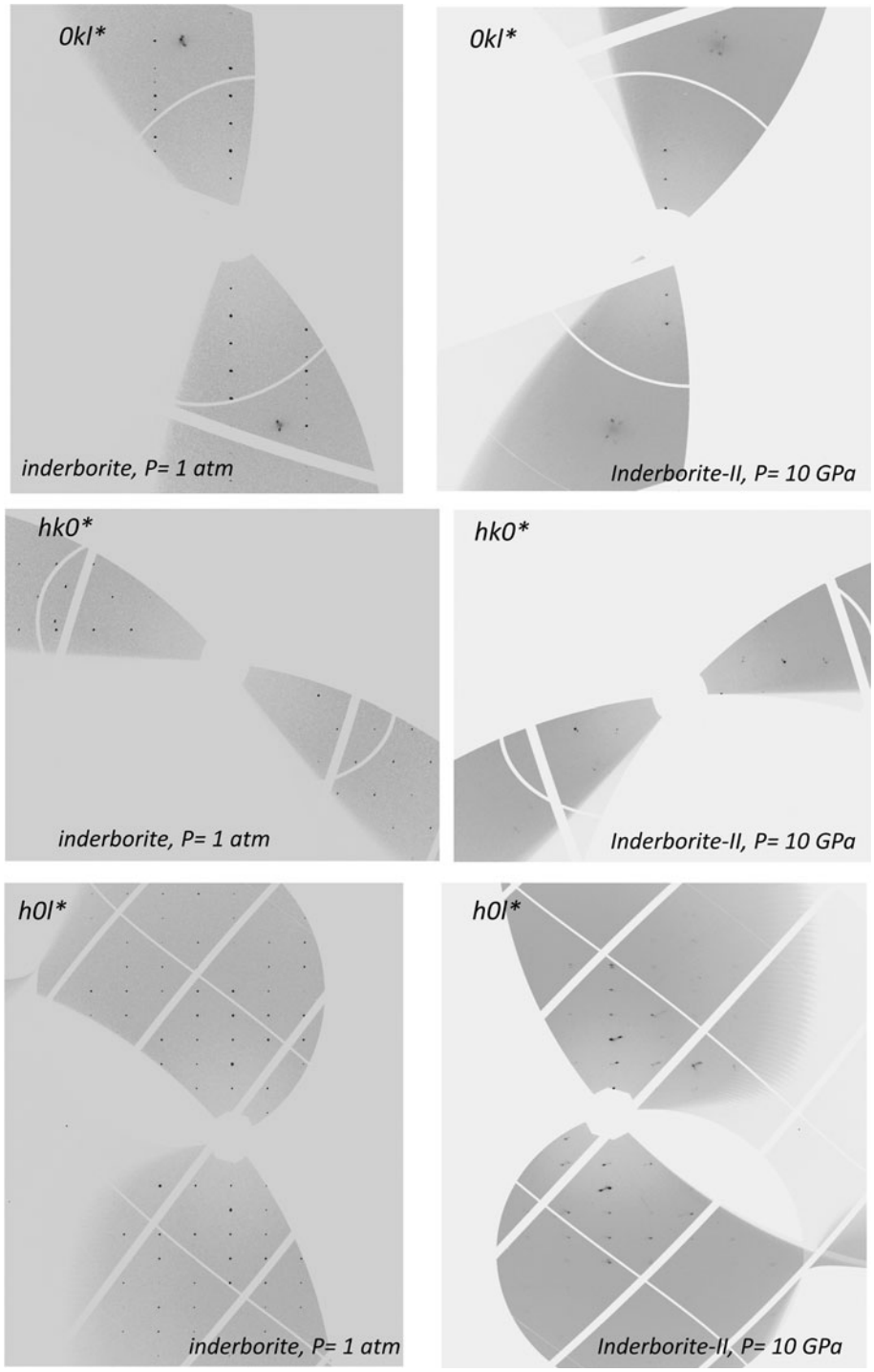

Figure 3. Reconstruction, based on the experimental data, of the *0kl**, *hk0** and *h0l** reciprocal lattice planes of inderborite- (left side) and inderborite-II (right side). Above the phase transition, the number of observed reflections dropped dramatically.

and $K''=\partial^2 K_{P0,T0}/\partial P^2$]. When truncated to the second order in energy, *i.e.* with $K'= \partial K_{P0,T0}/\partial P = 4$, the EoS transforms to:

$$P(fe) = 3K_{P0,T0}fe(1+2fe)^{5/2},$$

where *fe* [defined as $fe = \left[\left(\frac{V_0}{V}\right)^{\frac{2}{3}} - 1\right]/2$] is the Eulerian finite strain. The truncation to the second order in energy is reasonable when the experimental data plot following a horizontal trend in the diagram with Eulerian strain *vs*. 'normalised pressure' [*F*, defined as $F = P/[3fe(1+2fe)^{5/2}]$]. The BM–EoS parameters (listed in Table 3) were refined by minimising the differences between the EoS curves and the experimental data, which were weighted by their uncertainties in *P* and *V*. The fitting was carried out using the *EOS-FIT7-GUI* software (Angel *et al.*, 2014; Gonzalez-Platas *et al.*, 2016). An estimated uncertainty of ± 0.05 GPa was considered for pressure (Mao *et al.*, 1986) during the data fitting. The *fe vs F* plot is shown in Supplementary Fig. S1.

Results

Elastic behaviour

The linear elastic parameters, listed in Table 3, suggest that inderborite is a rather isotropic mineral, which deforms almost equally

https://doi.org/10.1180/mgm.2024.29 Published online by Cambridge University Press

Table 2. Evolution, with pressure, of some relevant interatomic angles (in °) and distances (*d* in Å) in inderborite structure [Δ defined as the difference between the value at 0.0001 GPa and that at 8.11 GPa].

P (GPa) Interatomic angles	O2–O3–O6	O1–O6–O4	O6–O1–O8	O8···O11···O9	O6···O7···O3	O5···O10···O4
0.0001	89.8(1)	165.7(1)	125.6(1)	132.2(2)	67.3(3)	121.2(4)
0.43(5)	89.3(1)	166.6(2)	125.0(1)	132.6(2)	67.3(1)	121.1(2)
0.61(5)	88.8(1)	166.8(2)	124.8(1)	132.2(3)	67.4(1)	121.1(2)
1.19(5)	88.3(1)	167.0(2)	124.7(1)	132.1(2)	67.5(1)	121.2(2)
1.80(5)	87.7(1)	167.4(2)	124.4(1)	131.6(3)	67.4(1)	121.2(2)
2.35(5)	86.9(1)	167.9(2)	124.2(1)	131.1(3)	67.9(1)	120.9(2)
2.82(5)	86.7(1)	168.2(2)	123.8(1)	131.1(3)	67.8(1)	121.2(2)
3.33(5)	86.0(1)	168.6(2)	123.5(1)	130.4(3)	68.1(1)	121.1(2)
3.84(5)	85.5(1)	169.0(2)	122.9(1)	130.3(3)	68.2(1)	121.1(2)
4.54(5)	85.0(1)	169.5(2)	122.4(1)	129.6(3)	68.2(1)	121.0(2)
6.23(5)	83.5(2)	170.7(2)	120.6(2)	128.0(3)	68.5(2)	121.0(3)
7.08(5)	82.7(2)	171.4(3)	120.2(2)	127.3(3)	68.6(2)	120.9(3)
7.80(5)	82.2(2)	172.0(3)	119.1(2)	126.8(3)	69.0(2)	120.9(3)
8.11(5)	82.0(2)	172.3(3)	118.6(2)	126.7(3)	69.2(2)	121.2(3)
Δ total	−7.8(3)	−6.6(4)	7.0(3)	5.5(5)	−1.9(5)	0.0(7)

P (GPa) Distances	O6···O7	O3···O7	O5···O10	O10···O4	O8···O11	O11···O9
0.0001	2.62(2)	2.867(9)	2.733(8)	2.79(2)	2.92(2)	3.10(2)
0.43(5)	2.639(4)	2.861(5)	2.723(6)	2.787(4)	2.898(5)	3.076(6)
0.61(5)	2.633(4)	2.859(5)	2.723(6)	2.779(4)	2.888(5)	3.083(6)
1.19(5)	2.611(4)	2.840(5)	2.713(6)	2.756(4)	2.862(5)	3.052(6)
1.80(5)	2.592(4)	2.820(5)	2.699(6)	2.732(4)	2.842(5)	3.034(6)
2.35(5)	2.576(4)	2.806(5)	2.692(6)	2.713(4)	2.824(5)	3.010(6)
2.82(5)	2.564(4)	2.789(5)	2.685(6)	2.697(4)	2.806(5)	2.982(6)
3.33(5)	2.550(4)	2.771(6)	2.669(6)	2.682(4)	2.797(5)	2.947(6)
3.84(5)	2.543(4)	2.773(6)	2.666(7)	2.671(4)	2.781(5)	2.926(7)
4.54(5)	2.529(4)	2.757(6)	2.658(6)	2.653(4)	2.770(5)	2.898(6)
6.23(5)	2.506(6)	2.719(7)	2.649(7)	2.613(6)	2.722(6)	2.873(7)
7.08(5)	2.501(6)	2.699(7)	2.646(8)	2.594(6)	2.712(6)	2.866(7)
7.80(5)	2.493(6)	2.677(7)	2.649(8)	2.579(6)	2.694(6)	2.866(7)
8.11(5)	2.487(6)	2.674(7)	2.638(8)	2.574(6)	2.684(6)	2.856(7)
Δ total	0.13(3)	0.19(2)	0.10(2)	0.22(3)	0.24(3)	0.24(3)

along the principal crystallographic directions. However, as expected in monoclinic crystals, the unit-cell angle β is free to vary with pressure, meaning that the linear bulk moduli along the principal crystallographic directions (listed in Table 3) do not actually describe the compressional anisotropy. To overcome this problem, the Eulerian finite strain analysis was performed with the *Win_Strain* software (Angel, 2011). The geometrical relationships between the unit-strain ellipsoid and the crystallographic axes of inderborite can be described by the following matrix (with $\varepsilon_1>\varepsilon_2>\varepsilon_3$):

$$\begin{pmatrix}\varepsilon_1\\ \varepsilon_2\\ \varepsilon_3\end{pmatrix} \angle \begin{pmatrix}79.8^\circ & 90^\circ & 10.8^\circ\\ 169.8^\circ & 90^\circ & 79.2^\circ\\ 90.0^\circ & 180^\circ & 90.0^\circ\end{pmatrix} \cdot \begin{pmatrix}a\\ b\\ c\end{pmatrix}$$

Table 3. Refined elastic parameters of the inderborite unit-cell and of the coordination polyhedrons, based on the isothermal II-BM Equation of State fit (*fixed parameter).

	V_0, x_0 (Å^3, Å)	$K_{V0,\ x0}$ (GPa)	K'	$\beta_{V0,\ x0}$ (GPa^{-1})
V	1731(1)	41(1)	4*	0.0244(6)
a	12.129(2)	44.6(6)	4*	0.0075(3)
b	7.4255(6)	47.5(4)	4*	0.0070(2)
c	19.195(2)	34.6(4)	4*	0.0096(3)
Ca–φ_8	26.1(7)	53(4)	4*	0.019(1)
Mg–φ_6	12.27(5)	81(8)	4*	0.012(1)
B1–φ_4	1.628(3)	260(30)	4*	0.0038(5)
B2–φ_4	1.643(3)	170(12)	4*	0.0059(4)

for inderborite, between 0.0001 and 8.11(5) GPa, ε_1:ε_2:ε_3 = 1.4:1.05:1 [$\varepsilon_1 = 0.00723(5)$ GPa^{-1}; $\varepsilon_2 = 0.00546(3)$ GPa^{-1}; and $\varepsilon_3 = 0.00524(4)$ GPa^{-1}]. The inderborite response to compression is only moderately anisotropic, with the major direction (ε_1) of compression describing an angle of only 10° with the *c* axis. This finding is surprising if compared to other hydrous borates, such as meyerhofferite (ε_1:ε_2:ε_3 = 5.8:4.7:1) or inyoite (ε_1:ε_2:ε_3= 3.5:2.1:1) (Comboni *et al.*, 2020a, 2022a). Regarding the high-pressure polymorph, the poor quality of the diffraction data did not allow any robust calculation, as discussed above. However, the previous matrix, showing the unit-strain ellipsoid calculated between 0.0001 and 8.11(5) GPa, does not describe the *P*-induced evolution of the strain ellipsoid itself, which undergoes a significant change as pressure increases. Initially, between 0.0001 and 2.35(5) GPa, the unit-strain ellipsoid is described by the following matrix:

$$\begin{pmatrix}\varepsilon_1\\ \varepsilon_2\\ \varepsilon_3\end{pmatrix} \angle \begin{pmatrix}49.6^\circ & 90^\circ & 40.9^\circ\\ 40.4^\circ & 90^\circ & 130.9^\circ\\ 90.0^\circ & 0^\circ & 90.0^\circ\end{pmatrix} \cdot \begin{pmatrix}a\\ b\\ c\end{pmatrix}$$

with ε_1:ε_2:ε_3 = 1.3:1.1:1 [$\varepsilon_1 = 0.0079(2)$ GPa^{-1}; $\varepsilon_2 = 0.0070(2)$ GPa^{-1}; and $\varepsilon_3 = 0.0062(1)$ GPa^{-1}]. Therefore, in the initial stage of compression, ε_1 and ε_2 lie on the *ac* plane, whereas ε_3 is parallel to *b*. However, as pressure increases, ε_1, ε_2 and ε_3 deviate from the

https://doi.org/10.1180/mgm.2024.29 Published online by Cambridge University Press

original orientation and, between 6.23(5) and 8.11(5) GPa, the unit-strain ellipsoid matrix changes to:

$$\begin{pmatrix} \varepsilon_1 \\ \varepsilon_2 \\ \varepsilon_3 \end{pmatrix} \angle \begin{pmatrix} 90.9^\circ & 90^\circ & 0.3^\circ \\ 90.0^\circ & 180^\circ & 90.0^\circ \\ 0.9^\circ & 90^\circ & 89.7^\circ \end{pmatrix} \cdot \begin{pmatrix} a \\ b \\ c \end{pmatrix}$$

with $\varepsilon_1:\varepsilon_2:\varepsilon_3 = 1.7:1:1$ [$\varepsilon_1 = 0.0063(2)$ GPa^{-1}; $\varepsilon_2 = 0.0037(6)$ GPa^{-1}; $\varepsilon_3 = 0.0036(5)$ GPa^{-1}]. Close to the phase transition, magnitude and orientation of the unit-strain ellipsoid differ from the earlier stages of compression, with ε_1 being almost parallel to *c*, ε_3 almost parallel to *a*, and ε_2 parallel to *b*.

Structure evolution

Referring to the first dataset (Table 1), between ambient pressure and 8.11(5) GPa, the length of the unit-cell edges of inderborite decreases steadily by ∼4.3% for the *a* and *b* unit-cell edges and by ∼3.3% along the *c* edge. The unit-cell volume decreases monotonically by ∼13.5% and the β angle steadily increases by ∼3.3% (see Table 1). Similar values (*i.e.* within 3σ) were observed for the second dataset. Up to 8.11(5) GPa, the crystal structure of inderborite deforms steadily with no significant changes. Between 8.11(5) and 8.80(5) GPa, inderborite undergoes a phase transition to its high-pressure polymorph, inderborite-II. This phase transition is rather disruptive, and data were collected only up to 10.10(5) GPa, as the number and intensity of the observed reflections [*i.e.* with $F_o^2 > 3\sigma(F_o^2)$] decreased significantly after the phase transition (down to ∼60). The phase transition is marked by a sharp volume decrease, typical of first-order phase transformations. Upon decompression, the crystal structure of inderborite does not revert to its ambient pressure polymorph, indicating that the transition is irreversible (at least for the time scale of our experiment).

Discussion

The high-quality structural refinements of inderborite with pressure allowed a full description of the main deformation mechanisms able to accommodate the effect of compression. The bulk modulus (K_{V0}) of the Bφ_4 tetrahedra, based on the isothermal Birch–Murnaghan Equation of State fit (Table 3), is more than five times higher than that of the inderborite unit cell. This suggests that the boron tetrahedrons act as uncompressible units, as expected at low–mid pressures (Table 3 and Supplementary Table S1). The same behaviour has been observed in all the hydrated borates studied so far at high pressure (*e.g.* ulexite, jadarite and kernite; Comboni *et al.*, 2020b, 2021a, 2022b) and in other minerals as well (*e.g.* reedmergnerite, londonite and barium metaborates, Gatta *et al.*, 2011; Bekker *et al.*, 2022; Gorelova *et al.*, 2022). On the other hand, the Mgφ_6 octahedra and Caφ_8 polyhedrons are significantly softer but with an important difference. The Ca-polyhedron compresses as expected, similar to observations in other hydrous borate crystal structures, such as meyerhofferite and inyoite, as evidenced by its bulk modulus (53(4) GPa) that is within 1σ of the values observed in meyerhofferite and inyoite (Comboni *et al.*, 2020a, 2022a). In contrast, the Mg-polyhedron is significantly stiffer with respect to Mg-polyhedra in other structures: the calculated bulk modulus in this study (81(8) GPa) is 11% higher than that of the same polyhedron in kurnakovite and ∼20% higher than that in inderite (67(4) GPa) (Pagliaro *et al.*, 2021; Comboni *et al.*, 2023). Although considerably stiff, the Mg–φ_6 polyhedron compression is highly anisotropic. In the experimental pressure range of this study, while the Mg–O9 and the Mg–O2 distances decrease by ∼1.8 and 1.5%, Mg–O8 decreases by ∼4%. This anisotropic compression, mainly affecting the Mg–O8 bond, leads to a progressive distortion of the Mg–φ_6 octahedron, as indicated by the progressive increase of the distortion index (σ^2) values (Supplementary Table S1). Overall, when compared to the bulk modulus of inderborite, all the polyhedrons are stiffer than the overall structure (see Table 3), meaning that the structural deformation in response to the applied pressure must be accommodated by other mechanisms. Indeed, tilting around the oxygen hinges between the B-, Ca- and Mg- polyhedrons can be deduced from the data in Table 2, which reports O–O–O angles that change significantly with pressure. In detail, the O2–$\widehat{O3}$–O6, O1–$\widehat{O6}$–O4 and O6–$\widehat{O1}$–O8 angles, which describe the degree of tilting between the $[B_3O_3(OH)_5]^{2-}$ polyion and the Ca–φ_8 octahedron, show a steady and progressive deformation as pressure increases [O2–$\widehat{O3}$–O6, O1–$\widehat{O6}$–O4 decrease by ∼7.8(2)° and 6.6(2)°, whereas O6–$\widehat{O1}$–O8 increases by ∼7.0(2)°]. The compression of the hydrogen-bonding network also accommodates part of the pressure-induced deformation and the interstitial ('zeolitic') H_2O molecule O11 might play a role in the destabilisation of the crystal structure. This molecule is connected, via hydrogen bonding, with the O8 hydroxyl group and the O9 H_2O molecules (Fig. 1, Supplementary Fig. S2). At ambient pressure, the interatomic angle O8···$\widehat{O11}$···O9 is 132.2(2)°, and it only remains roughly constant in the very first GPa of compression, decreasing progressively with increasing pressure (Table 2). This is paired with a steady decreasing of the O11···O9 and O11···O8 distances (Table 2), which decrease by ∼8.4 and 7.9%. These are not the only atoms of oxygen connected *via* hydrogen bonding affected by the structure deformation. Indeed, the interatomic O6···$\widehat{O3}$···O7 angle, which is formed by the oxygen atom O7 (being part of the B2-tetrahedron), *acceptor* of two hydrogen bonds from the hydroxyl groups O3 and O6 (which belong to the Ca-polyhedron), deforms steadily as pressure increases (Table 2). In addition O11···O9 and O11···O8, together with the interatomic distances O6···O7 and O7···O3, decrease drastically with pressure (of ∼5 and 6.7%, Table 2). The H_2O molecule O10 is the *donor* of two hydrogen bonds, with O4 and O5 as *acceptors* (Supplementary Fig. S2), two atoms of oxygen that act as hinges in the $[B_3O_3(OH)_5]^{2-}$ polyion. The interatomic angle O5···$\widehat{O10}$···O4 remains unchanged (within 1σ) up to 8.11(5), GPa, however the distances between the *acceptors* (O4 and O5) and the *donor* (O10) progressively decrease of ∼7.9 and 3.7%, respectively. Therefore, the interaction between the oxygen pairs O10···O4 and O10···O5 increases steadily with pressure. The compression of the hydrogen bond network is significantly larger with respect to the average decrease of the Ca–O, Mg–O and B–O distances (∼4%, ∼2% and ∼1.6%, respectively), further highlighting that the main mechanisms with which the structure deforms are (1) the tilting around inter-polyhedral oxygen hinges and (2) compression of the hydrogen bonding network. This phenomenon is analogous to what was observed in several other hydrated borate structures characterised by a pervasive hydrogen bonding network, which plays a paramount role in the stability of the crystalline edifice (*e.g.* meyerhofferite and inyoite; Comboni *et al.*, 2021b, 2022a). It is likely that the combination of these two deformation mechanisms induces the changes of the orientation of the unit strain ellipsoid, ultimately affecting the elasticity and the (very moderate)

https://doi.org/10.1180/mgm.2024.29 Published online by Cambridge University Press

anisotropy of inderborite. Supplementary Fig. S4 shows the evolution of the O···O distance (reported in Table 2) with pressure. Note that the slopes of such trends change manifestly with pressure, so this can be correlated potentially to the changes in the unit-strain ellipsoid configuration, highlighting, once again, the role of the hydrogen-bonding network on the stability of the crystal structure.

Concluding remarks

In this study, we have investigated the high-pressure behaviour of inderborite through *in situ* single crystal X-ray diffraction, up to ~10 GPa. Data collected at high-pressure revealed that:

(1) The ambient-condition polymorph of inderborite remains stable up to ~8 GPa. Between 8.11(5) and 8.80(5) GPa, inderborite undergoes a first-order phase transition. The space group of inderborite-II, which is metrically monoclinic, remains unclear. The phase transition (which is not reversible) is marked by a volume decrease of ~7.0%.
(2) The elastic parameters of inderborite have been determined, and the elastic behaviour has been described in detail. These data will contribute to improving the thermodynamic database of hydrous borates.
(3) With increasing pressure, the volume compression is accommodated primarily by the deformation (and compression) of the hydrogen bonding network, as well as by the tilting of the Ca-, Mg- and B- polyhedrons around the bridging oxygen sites.
(4) The pressure at which the inderborite-to-inderborite-II phase transition occurs (8.5 ± 0.40 GPa) follows the trend observed in most hydrated borates studied so far (Comboni *et al.*, 2020a, 2021a, 2022a; Pagliaro *et al.*, 2021), excluding inderite (Comboni *et al.*, 2023). This finding strengthens the presumed correlation between the pressure at which the phase transition occurs and the total H_2O content (in wt.%, Supplementary Fig. S3).
(5) The bulk modulus of inderborite ($K_{V0} = 41(1)$ GPa) is similar to the bulk modulus of quartz (~37 GPa) and lower than those of other aggregates used in radiation shielding concretes (*e.g.* colemanite $K_{V0} = 67(4)$; Okuno, 2005; Lotti *et al.*, 2017). Similarly to colemanite and inderite, inderborite is a Na-free borate, meaning that it cannot promote ASR reactions (*i.e.* 'alkali-silica reactions'; Thomas, 2011; Figueira *et al.*, 2019; Mohammadi *et al.*, 2020), which are known to undermine the durability of Portland cements. Considering the stability field of inderborite at high pressure and its elastic parameters, this borate can potentially be used as a B-rich aggregate in radiation-shielding materials.

Acknowledgements. ESRF is thanked for the allocation of the beamtime (proposal MA-5273, doi: 10.15151/ESRF-ES 656089266). GDG, DC, PL and TB acknowledge the support of the Italian Ministry of Education (MIUR) through the project "*PRIN2017 - Mineral reactivity, a key to understand large-scale processes*" (2017L83S77) and of the University of Milan through the project *Piano di Sostegno alla Ricerca 2022*. The work was partly supported by the Italian Ministry for Universities and Research (MUR) through the project "Dipartimenti di Eccellenza 2023–2027".

Supplementary material. The supplementary material for this article (Figs S1–4 and Table S1) can be found at https://doi.org/10.1180/mgm.2024.29.

Competing interests. The authors declare none.

References

Abe T. (1952) Borosilicate glasses. *Journal of the American Ceramic Society*, **35**, 284–299.

Angel R.J. (2011) *Win_Strain. A program to calculate strain tensors from unit-cell parameters*. <http://www.rossangel.com/home.htm> [downloaded 27 September 1991].

Angel R.J., Gonzalez-Platas J. and Alvaro M. (2014) EosFit7c and a Fortran module (library) for equation of state calculations. *Zeitschrift fur Kristallographie*, **229**, 405–419.

Baur W.H. (1974) The geometry of polyhedral distortions. Predictive relationships for the phosphate group. *Acta Crystallographica*, **B30**, 1195–1215.

Baysal O. (1973) New hydrous magnesium-borate minerals in kurnakovite, inderite, inderborite turkey. *Bulletin of the Mineral Research and Exploration*, **80**, 93–103.

Bekker T.B., Podborodnikov I. V., Sagatov N.E., Shatskiy A., Rashchenko S., Sagatova D.N., Davydov A. and Litasov K.D. (2022) γ-BaB_2O_4: high-pressure high-temperature polymorph of barium borate with edge-sharing BO_4 tetrahedra. *Inorganic Chemistry*, **61**, 2340–2350.

Birch F. (1947) Finite elastic strain of cubic crystals. *Physical Review*, **71**, 809–824.

Birsoy R. and Özbaş Ü. (2012) Activity diagrams of borates: Implications on common deposits. *Carbonates and Evaporites*, **27**, 71–85.

Burns P.C. and Hawthorne F.C. (1994) Structure and hydrogen bonding in inderborite, a heteropolyhedral sheet structure. *The Canadian Mineralogist*, **32**, 533–539.

Carter R.S., Palevsky H., Myers V.W. and Hughes D.J. (1953) Thermal neutron absorption cross sections of boron and gold. *Physical Review*, **92**, 716–721.

Chen S., Ai L., Zhang T., Liu P., Liu W., Pan Y. and Liu D. (2020) Synthesis and application of a triazine derivative containing boron as flame retardant in epoxy resins. *Arabian Journal of Chemistry*, **13**, 2982–2994.

Comboni D., Pagliaro F., Gatta G.D., Lotti P., Battiston T., Garbarino G. and Hanfland M. (2020a) High-pressure behaviour and phase stability of $Ca_2B_6O_6(OH)_{10}{\cdot}2(H_2O)$(meyerhofferite). *Physics and Chemistry of Minerals*, **47**, https://doi.org/10.1007/s00269-020-01117-3

Comboni D., Pagliaro F., Gatta G.D., Lotti P., Milani S., Merlini M., Battiston T., Glazyrin K. and Liermann H. (2020b) High-pressure behavior and phase stability of $Na_2B_4O_6(OH)_2{\cdot}3H_2O$ (kernite). *Journal of the American Ceramic Society*, **103**, 5291–5301.

Comboni D., Pagliaro F., Gatta G.D., Lotti P., Battiston T., Merlini M. and Hanfland M. (2021a) Phase transition and high-pressure behavior of ulexite, a potential aggregate in radiation-shielding concretes. *Construction and Building Materials*, **291**, 123188.

Comboni D., Poreba T., Pagliaro F., Battiston T., Lotti P., Gatta G.D. and Garbarino G. (2021b) Crystal structure of the high-P polymorph of $Ca_2B_6O_6(OH)_{10} \cdot 2(H_2O)$ (meyerhofferite). *Acta Crystallographica*, **B6**, 940–945.

Comboni D., Battiston T., Pagliaro F., Lotti P., Gatta G.D. and Hanfland M. (2022a) High-pressure behaviour and atomic-scale deformation mechanisms in inyoite, $CaB_3O_3(OH)_5{\cdot}4H_2O$. *Physics and Chemistry of Minerals*, **49**, 1–10.

Comboni D., Battiston T., Rumsey M.S., Pagliaro F., Lotti P., Hanfland M. and Gatta G.D. (2022b) High-pressure behavior and phase transition of jadarite, a promising B and Li mineral commodity. *Journal of the American Ceramic Society*, **105**, 7011–7021.

Comboni D., Poreba T., Battiston T., Hanfland M. and Gatta G.D. (2023) On the anomalous high-pressure phase transition of inderite, $MgB_3O_3(OH)_5{\cdot}5H_2O$. *Solid State Sciences*, **140**, 107187.

European Commission (2014) *Communication from the Commission: On the Review of the List of Critical Raw Materials for the EU and the Implementation of the Raw Materials Initiative*. COM no. 297, European Commission: Brussels.

Figueira R.B., Sousa R., Coelho L., Azenha M., de Almeida J.M., Jorge P.A.S. and Silva C.J.R. (2019) Alkali-silica reaction in concrete: Mechanisms, mitigation and test methods. *Construction and Building Materials*, **222**, 903–931.

García-Veigas J. and Helvacı C. (2013) Mineralogy and sedimentology of the Miocene Göcenoluk borate deposit, Kirka district, western Anatolia, Turkey. *Sedimentary Geology*, **290**, 85–96.

Gatta G.D., Vignola P. and Lee Y. (2011) Stability of (Cs, K)$Al_4Be_5B_{11}O_{28}$ (londonite) at high pressure and high temperature: A potential neutron absorber material. *Physics and Chemistry of Minerals*, **38**, 429–434.

Gatta G.D., Cannaò E., Comboni D., Battiston T. and Fabelo O. (2023) A neutron diffraction study of the hydrous borate inderborite, $CaMg[B_3O_3(OH)_5]_2(H_2O)_4{\cdot}2H_2O$. *American Mineralogist*, in press, 10.2138/am-2023-9162.

Glinicki M.A., Antolik A. and Gawlicki M. (2018) Evaluation of compatibility of neutron-shielding boron aggregates with Portland cement in mortar. *Construction and Building Materials*, **164**, 731–738.

Gonzalez-Platas J., Alvaro M., Nestola F. and Angel R. (2016) EosFit7-GUI: A new graphical user interface for equation of state calculations, analyses and teaching. *Journal of Applied Crystallography*, **49**, 1377–1382.

Gorelova L., Pakhomova A., Aprilis G., Yin Y., Laniel D., Winkler B., Krivovichev S., Pekov I., Dubrovinskaia N. and Dubrovinsky L. (2022) Edge-sharing BO_4 tetrahedra and penta-coordinated silicon in the high-pressure modification of $NaBSi_3O_8$. *Inorganic Chemistry Frontiers*, **9**, 1735–1742.

Hanfland M. (2016) Crystallography at high pressure using synchrotron radiation. *Synchrotron Radiation in Natural Science*, **15**, 30–31 [Extended abstract https://synchrotron.org.pl/publ/biulet/vol015/044-045_v15.pdf].

Hawthorne F.C. (2012) A bond-topological approach to theoretical mineralogy: Crystal structure, chemical composition and chemical reactions. *Physics and Chemistry of Minerals*, **39**, 841–874.

Helvacı C. and Palmer M.R. (2017) Origin and distribution of evaporate borates – the primary economic sources of boron. *Elements*, **13**, 249–254.

Helvaci C. and Alonso R.N. (2000) Borate deposits of Turkey and Argentina; A summary and geological comparison. *Turkish Journal of Earth Sciences*, **9**, 1–27.

Kistler R.B. and Helvacı C. (1994) Boron and Borates. Pp. 171–186 in: *Industrial Minerals and Rocks* (D. Carr, editor). 6th edition. Society for Mining, Metallurgy and Exploration, Littleton, CO, USA.

Klotz J.H. and Moss J.I. (1996) Oral toxicity of a boric acid - Sucrose water bait to Florida carpenter ants (Hymenoptera: Formicidae). *Journal of Entomological Science*, **31**, 9–12.

Klotz S., Chervin J.C., Munsch P. and Le Marchand G. (2009) Hydrostatic limits of 11 pressure transmitting media. *Journal of Physics D: Applied Physics*, **42**.

Kurkutova E., Rumanova I.M. and Belov N. (1965) Crystal structure of inderborite $CaMg[B_3O_3(OH)_5]_2{\cdot}6(H_2O)$. *Soviet Physics Doklady*, **164**, 90.

Lotti P., Gatta G.D., Comboni D., Guastella G., Merlini M., Guastoni A. and Liermann H.-P. (2017) High-pressure behavior and P-induced phase transition of $CaB_3O_4(OH)_3{\cdot}H_2O$ (colemanite). *Journal of the American Ceramic Society*, **100**, 2209–2220.

Mao H.K., Xu J. and Bell P.M. (1986) Calibration of the ruby pressure gauge to 800 kbar under quasi-hydrostatic conditions. *Journal of Geophysical Research*, **91**, 4673.

Mohammadi A., Ghiasvand E. and Nili M. (2020) Relation between mechanical properties of concrete and alkali-silica reaction (ASR); a review. *Construction and Building Materials*, **258**, 119567.

Momma K. and Izumi F. (2008) VESTA: A three-dimensional visualization system for electronic and structural analysis. *Journal of Applied Crystallography*, **41**, 653–658.

Okuno K. (2005) Neutron shielding material based on colemanite and epoxy resin. *Radiation Protection Dosimetry*, **115**, 258–261.

Okuno K., Kawai M. and Yamada H. (2009) Development of novel neutron shielding concrete. *Nuclear Technology*, **168**, 545–552.

Pagliaro F., Lotti P., Battiston T., Comboni D., Gatta G.D., Cámara F., Milani S., Merlini M., Glazyrin K. and Liermann H. (2021) Thermal and compressional behavior of the natural borate kurnakovite, $MgB_3O_3(OH)_5{\cdot}5H_2O$. *Construction and Building Materials*, **266**, 121094.

Palmer M. and Swihart G. (1996) Boron isotope geochemistry: An overview. Pp. 709–744 in: *Boron: Mineralogy, Petrology, and Geochemistry* (L. Anovitz and E. Grew, editors). Mineralogical Society of America, Washington, DC.

Palmer M.R. and Helvaci C. (1997) The boron isotope geochemistry of the neogene borate deposits of western Turkey. *Geochimica et Cosmochimica Acta*, **61**, 3161–3169.

Petrícek V., Dušek M. and Palatinus L. (2014) Crystallographic computing system JANA2006: General features. *Zeitschrift fur Kristallographie*, **229**, https://doi.org/10.1515/zkri-2014-1737

Poreba T., Comboni D., Mezouar M., Hanfland M. and Garbarino G. (2022) Tracking of structural phase transitions via single crystal X-ray diffraction at extreme conditions: advantages of extremely brilliant source. *Journal of Physics: Condensed Matter*, **35**.

Rigaku Oxford Diffraction (2019) *CrysAlisPro Software system, version 1.171.40.67a*. Wroclaw, Poland.

Robinson K., Gibbs G. V and Ribbe P.H. (1971) Quadratic elongation: a quantitative measure of distortion in coordination polyhedra. *Science*, **172**, 567–570.

Thomas M. (2011) The effect of supplementary cementing materials on alkali-silica reaction: A review. *Cement and Concrete Research*, **41**, 1224–1231.

U.S.G.S. (2022) *Mineral Commodity Summaries 2022*. United States Geological Survey, Reston, Virginia, USA, 202 pp.

Woods W.G. (1994) An introduction to boron: History, sources, uses, and chemistry. *Environmental Health Perspectives*, **102**, 5–11.

Yu S., Wang X., Pang H., Zhang R., Song W., Fu D., Hayat T. and Wang X. (2018) Boron nitride-based materials for the removal of pollutants from aqueous solutions: A review. *Chemical Engineering Journal*, **333**, 343–360.

Zheng M.-P., Qi W. and Yuan H.-R. (2005) Characteristics of salt lake boron deposits and magnesium borate deposits of the Qinghai-Tibet Plateau, China. *Mineral Deposit Research: Meeting the Global Challenge*, **30**, 1123–1125.

https://doi.org/10.1180/mgm.2024.29 Published online by Cambridge University Press